that m-IGRT image registration using PET-based reconstructed planar images along the in-plane direction is feasible for clinical use if PDRI registration is performed at two orthogonal gantry angles.

(Some figures in this article are in colour only in the electronic version)

1. Introduction

Image guided radiotherapy (IGRT) techniques are presently used clinically to improve the accuracy of treatment delivery in photon radiation therapy. IGRT is used to correct for patient positioning errors prior to or during treatment by using image guided procedures. Patient setup can be verified through the co-registration of digitally reconstructed radiographs (DRR) and imaging plate (IP) or electronic portal imaging device (EPID) images taken using MV-x rays from a linear accelerator (Linac) while the patient is set up just prior to treatment (Dong and Boyer 1995, Gilhuijs *et al* 1996). Linac systems with on-board cone-beam computed tomography (CBCT) devices have also been developed (Pouliot *et al* 2005, Jaffray *et al* 2002, Groh *et al* 2002, Ford *et al* 2002, Munbodh *et al* 2006). CBCT allows the imaging of the target volume and organs at risk during treatment. Accuracy of patient setup verification error is important in order to ensure that the actual treatment geometry is as close as possible to the treatment planning geometry. At present, patient setup verification is done mostly by the alignment of bony structures in radiographic images taken during treatment and those used for treatment planning. The change in the tumor size and location inside the body is usually difficult to determine during treatment. Making the tumor visible in the irradiation field is thus desirable in order to improve setup verification accuracy.

Positron emission tomography (PET) based on sugar metabolism in the tumor caused by ^{18}F-fluorodeoxyglucose (FDG) uptake has been shown to be effective for distinguishing the tumor during diagnosis (Som *et al* 1980). Since PET images are functional images, they allow cell activity to be visible; thus, the tumor position can be determined. Another promising radioactive tracer for PET imaging is ^{18}F-fluoromisonidazole (FMISO) (Nehmeh *et al* 2008). FMISO is able to delineate hypoxic cells, which are known to be radiation resistant, in tumors. Clinical trials have demonstrated improved tumor control by delivering escalated doses to hypoxic tumor cells using IMRT and other techniques (Lee and Le 2008).

The spatial resolution and sensitivity of recent PET devices have also been significantly improved. This has been partly due to (1) the development of new detector elements such as BGO or GSO crystals, (2) the change in the acquisition method from 2D to 3D, and (3) the invention of depth-of-interaction (DOI) (Wienhard *et al* 2002, Yamaya *et al* 2003). The application of PET technology as a new modality for diagnostic procedures is also now being considered, for example, positron emission mammography (PEM) (Smith *et al* 2003, Huesman *et al* 2000, Zhang *et al* 2007, Raylman *et al* 2008, MacDonald *et al* 2009). In this study, we propose a PET-based molecular image guided radiation therapy (m-IGRT) system for patient setup verification in cases where significant tumor shrinkage or growth may occur, such as intracranial or head and neck. In the practical implementation of an m-IGRT system, it is preferable that the PET device is combined with a radiotherapy gantry to guarantee mechanical precision. There are, however, some restrictions on how the PET detectors can be mounted to the present gantry systems.

Because PET is a device that detects the annihilation radiation caused by positrons, it is necessary that at least a pair of opposed detectors are arranged to detect the two photons simultaneously. It is preferable that the isocenter of the pair of opposed detectors is identical to the isocenter of the radiotherapy unit. A structure with a wide open space between a pair of

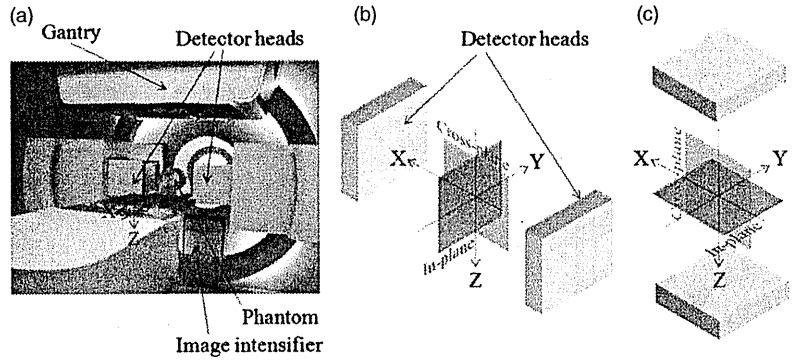

Figure 1. (a) The BOLPs with its gantry positioned at 0°. (b) The orientations of the in-plane and cross-plane directions in the BOLPs at a gantry angle of 0°. (c) The orientations of the in-plane and cross-plane directions in the BOLPs at a gantry angle of 90°.

opposed detectors is also needed so that the mega-voltage irradiation field does not become obstructed. The gantry rotation of the radiotherapy unit and the movement or the rotation of the couch must also be considered. Moreover, it is necessary to secure a wide field of view to use the device for setup verification. However, it is difficult in the conventional PET detector geometry, with ring-shape arrangement, to achieve this purpose. We therefore selected a geometry with a pair of opposing parallel-plane detectors. The advantage of this detector geometry is that it is structurally simple, and that it can be mounted easily on a radiotherapy gantry, similar to on-board imaging (OBI) devices.

In order to evaluate the feasibility of molecular image guided registration, we used the beam on-line PET system (BOLPs), developed at the Particle Therapy Division of the National Cancer Center, Kashiwa (Nishio *et al* 2005, 2006, 2010). The system consists of a pair of opposing parallel-plane detectors mounted on the gantry which can detect annihilation radiation produced by positron emitters (e.g. ^{15}O, ^{14}O, ^{13}N and ^{11}C). The BOLPs was originally developed for visualizing irradiation fields by measuring the activity of positron emitters which are generated by nuclear reactions from incident proton beams. The BOLPs has the same detector configuration as that of our proposed system.

In this paper, we report on the feasibility of a novel m-IGRT by comparing the PET-based digitally reconstructed planar image (PDRI) registration with radiographic registration.

2. Materials and method

2.1. Beam on-line PET system

The BOLPs at the National Cancer Center, Kashiwa, in Japan was used to verify the accuracy of patient setup verification in our proposed parallel-plane PET system. The BOLPs detector is mounted at the gantry of the proton irradiation system as shown in figure 1(a). The detector head consists of 3960 BGO crystals (2 mm × 2 mm × 20 mm) covering a 16 × 16 cm^2 field of view. The distance between the detector heads was fixed at 40 cm. Shown in figure 1(b) are the orientations of the in-plane and cross-plane directions for a gantry angle of 0°. The orientations of the in-plane and cross-plane directions for a gantry angle of 90° are illustrated in figure 1(c). The evaluation of the full width at half maximum (FWHM) of the profile of

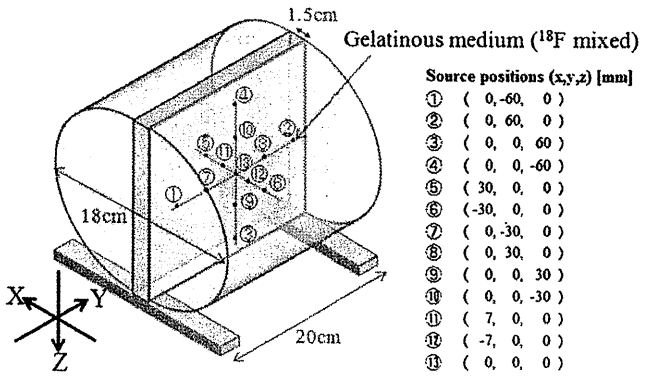

Figure 2. Cylindrical phantom with ^{18}F-sources placed in the positions as indicated.

2 mm diameter sources was done along the cross-plane and in-plane directions for a gantry angle of 0°. The FWHM of the profile is indicative of the spatial resolution.

In the image registration, only the reconstructed in-plane image from the parallel-plane PET data was used, and from here on, this in-plane image will be referred to as PDRI.

The BOLPs also includes an on-board x-ray system that allows the acquisition of radiographic images for patient setup verification. We compared the accuracy of radiographic and PDRI registrations.

2.2. Image reconstruction method

The detector configuration of the BOLPs is different from that of conventional PET systems in that they do not encircle the subject. Due to the parallel placement of the detector heads, there is limited angular sampling and loss of line of response (LOR) and the usual sinogram-based reconstruction method is not applicable. Therefore, the maximum likelihood-expectation maximization (MLEM) method (Shepp and Vardi 1982) was used in the LOR-based reconstruction using Siddon's algorithm (Siddon 1985).

In this study, only the detector sensitivity correction was applied while ignoring the other possible correction factors to account for scattering or absorption.

2.3. Phantom configuration

Two custom-made phantoms were used in our measurements. The first phantom was a polycarbonate cylindrical phantom with a width of 20 cm and a diameter of 18 cm. We refer to this phantom as the *cylindrical phantom*. It contained 13 cylindrical radiation sources (each with a diameter of 2 mm and width of 2 mm) that were arranged as shown in figure 2. The other phantom was a polycarbonate plate containing five cylindrical radiation sources of various diameters (i.e. 8, 12, 16, 24, 32 mm) with 1.5 cm width, representing different tumor sizes as shown in figure 3(a). This was attached to an acrylic slab (height: 20 cm, width: 18.5 cm, depth: 0.3 cm) as shown in figure 3(b). In this paper, we refer to this phantom setup as the *tumor phantom*. The radiation sources in both the cylindrical phantom and the tumor phantom used ^{18}F that was homogeneously mixed in a gelatinous medium.

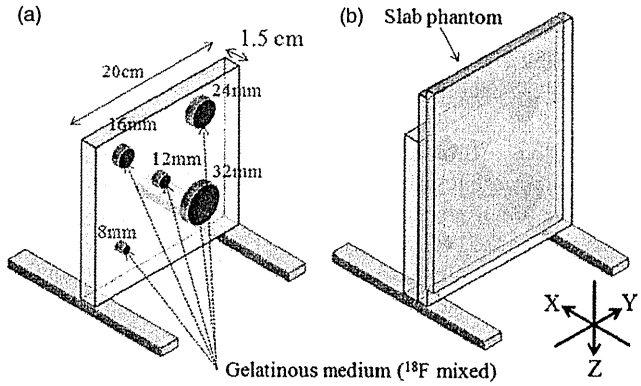

Figure 3. (a) Polycarbonate plate containing ^{18}F-sources of various diameters representing different tumor sizes. (b) The plate in (a) attached to an acrylic slab phantom.

2.4. FWHM of the profile of 2 mm diameter sources

The unique detector geometry of the BOLPs does not allow the use of the filtered back projection reconstruction as specified in the National Electrical Manufactures Association (NEMA) standard which is used for the evaluation of PET detectors. Therefore we used a modified method for image reconstruction based on PEM (Smith *et al* 2004, MacDonald *et al* 2009), which has a detector geometry similar to the BOLPs. PEM devices and the BOLPs have anisotropic spatial resolutions because the detectors do not encircle the object and do not rotate to acquire the full 360° angular sampling required for full three-dimensional tomography. Parallax error caused by the thickness of scintillation crystals is considered (Hoffman *et al* 1989, Lerche *et al* 2005).

We evaluated the FWHM of the profile of 13 cylindrical sources with a diameter of 2 mm and width of 2 mm using the cylindrical phantom shown in figure 2. The ^{18}F activity was 40 kBq ml^{-1}. The projection data were measured for 15 min at a gantry angle of 0°. The image reconstruction via the MLEM method was applied with the pixel size and slice thickness of 1.00 mm and a reconstruction volume of 15 × 15 × 15 cm^3.

2.5. Registration experiments

2.5.1. PDRI registration. PDRI registration was performed by comparing the in-plane digitally reconstructed planar image from the BOLPs and the image obtained from a conventional PET (Discovery ST, General Electric, Schenectady, New York). The pixel size and slice thickness were 3.91 and 3.27 mm, respectively. We placed the tumor phantom in a conventional PET such that the polycarbonate plate was parallel to the longitudinal axis and the center of the plate aligned with the isocenter. Data collection was performed for 15 min.

The tumor phantom was then placed at the isocenter of the BOLPs to obtain the data for the PDRI. Data were also collected for two additional conditions where the tumor phantom was displaced by 2 and 7 mm along the *Y*-axis, away from the isocenter to avoid the observer's bias from trial learning. Each measurement with the BOLPs was carried out for 5 min. The activity of ^{18}F was 20 kBq ml^{-1} and the background activity was 4 kBq ml^{-1}. The gantry angle was fixed at 0°. MLEM image reconstruction was applied with the pixel size and slice thickness of 1.00 mm and a reconstruction volume of 15 × 15 × 5 cm^3. PDRIs corresponding

to 1, 3 and 5 min measurements were generated for each setup position. Image registration based on the PDRI for each setup position was performed by five observers. The reference image was reconstructed from a conventional PET image.

2.5.2. Radiographic registration. To compare the accuracy of radiographic and PDRI registrations, we also performed image registration using images obtained from an x-ray CT and a fluoroscopic system. The tumor phantom was placed at the isocenter of the x-ray CT following the same setup as used in the PET measurement. The pixel size and slice thickness were 0.98 and 1.25 mm, respectively. Fluoroscope images of the tumor phantom were also taken using the installed fluoroscopic system in the proton irradiation system. The position of the tumor phantom was subsequently moved along the *Y*-axis to take additional data at 2 and 7 mm from the isocenter. The reference image used in the radiographic registration was the DRR reconstructed from x-ray CT.

2.5.3. Registration accuracy evaluation. To evaluate the accuracy of the registration methods, image registration trials using in-house software were performed for ten trials. Each trial consisted of five different images shown twice to the observers. Five observers estimated the shifts in each trial. From the image registration data, we calculated the registration error (RE) using equation (1). Actual shift (Y_{actual}) was 0, 2 and 7 mm along the *Y*-axis. Z_{obs} and Y_{obs} in the equation refer to the observed translation along the *Z*-axis and *Y*-axis respectively performed by the five subjects. Statistical analysis was performed based on the registration error for both the radiographic and PDRI registrations:

$$\text{RE(mm)} = \sqrt{(Z_{\text{obs}})^2 + (Y_{\text{obs}} - Y_{\text{actual}})^2}. \tag{1}$$

Here RE denotes the registration error, Z_{obs} the observed translation along the *Z*-axis, Y_{obs} the observed translation along the *Y*-axis and Y_{actual} the actual setup couch translation along the *Y*-axis (0, 2, 7 mm).

2.5.4. Statistical analysis. Statistical analysis of our data was performed using JMP 8 (SAS Institute Inc.) software. The mean registration error and standard deviation (SD) for the various diameters were determined based on the acquisition time for data collection (i.e. 1, 3 and 5 min) and modality (BOLPs, x-ray fluoroscopy). Data were analyzed by one-way ANOVA, while the differences among means were analyzed by two-sided Student's *t*-test with the level of statistical significance set to $p < 0.05$.

3. Results

3.1. FWHM of the profile of 2 mm diameter sources

Figure 4 shows the reconstructed in-plane and cross-plane images of the cylindrical phantom corresponding to a gantry angle of 0°. The reconstructed source diameter at the central position was larger than the others due to blurring caused by adjacent sources. The FWHM of each radiation source is shown in figure 5. The mean ± SD for FWHM was 1.8 ± 0.3 mm in the in-plane image and 8.1 ± 1.2 mm in the cross-plane image at a gantry angle of 0°.

3.2. Registration accuracy evaluation

Shown in figure 6 are the PDRIs of the tumor phantom at a gantry angle of 0°. Images from left to right correspond to the three acquisition times (1, 3 and 5 min) for data collection,

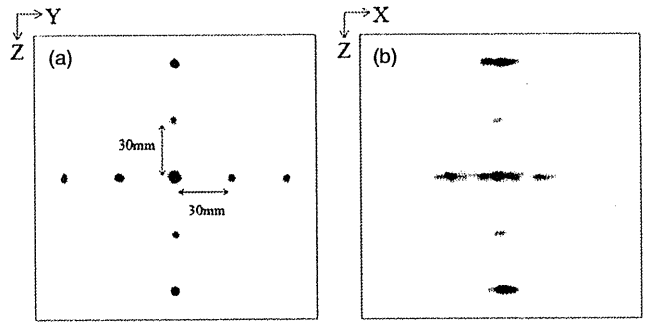

Figure 4. Planar images of the ^{18}F-sources along the (a) in-plane and (b) cross-plane directions reconstructed from the BOLPs data at a gantry angle of 0°.

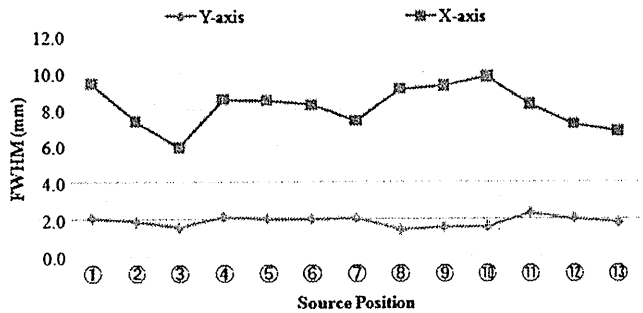

Figure 5. FWHM of the profile of the 2 mm diameter sources in the cylindrical phantom of figure 2.

while those from top to bottom correspond to the positions of the phantom (0, 2 and 7 mm) during data acquisition. The gray-scale window level of the images was adjusted to enhance the contrast. The measured activity at the source increased linearly as a function of acquisition time, and contrast to the background was constant and no inconsistency was observed among the three positions.

Figure 7 shows the variations in the observed PDRI and radiographic registration errors with respect to the acquisition time, phantom position and source diameter. PDRI registration errors were obtained from the registration of the reconstructed PET and BOLPs planar images. The radiographic registration errors were obtained from registration of DRR and portal (x-ray) images. The dependence of the registration error on the phantom position was not seen for each diameter.

Shown in table 1 are the mean $\pm$ SD of the registration errors based on our ANOVA. For the diameter of 8 mm the mean registration error of the PDRI registration appears to be influenced by the acquisition time with the longest acquisition time having the least mean registration error. The registration error for the radiographic registration was comparable to that of the shortest acquisition time of 1 min for the PDRI. The differences in the registration error between the image registration modalities listed in table 1 for the 8 mm diameter were found to be significant at a p-value of <0.0001. On the other hand, the mean registration error in all four registration methods for the diameter of 12 mm was found to be statistically insignificant ($p = 0.3545$) with their mean registration error ranging between 0.49 and 0.63. For diameters of 16 and 24 mm, the three acquisition times using the PDRI resulted in similar

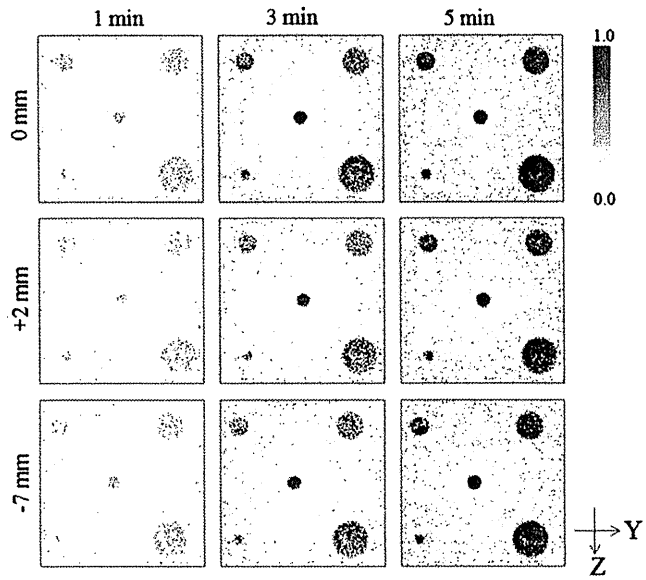

Figure 6. Planar image reconstructions of the ^{18}F-sources in the tumor phantom of figure 3(b). Shown are the results for three phantom positions relative to the isocenter and at the acquisition times of 1 , 3 and 5 min, respectively.

Table 1. Statistical comparison of registration errors from PDRI and radiographic registrations using ANOVA. PDRI registration was performed using reconstructed planar images from PET data (at the acquisition time of 15 min) and BOLPs data (at the acquisition times of 1, 3 and 5 min). Radiographic registration was performed using DRR and portal (x-ray) images.

	Diameter				
Registration method	8 mm	12 mm	16 mm	25 mm	32 mm
PDRI (1 min)	1.07 ± 0.42	0.49 ± 0.34	1.02 ± 0.44	1.28 ± 0.35	1.12 ± 0.39
PDRI (3 min)	0.87 ± 0.29	0.59 ± 0.24	1.01 ± 0.38	1.25 ± 0.29	0.86 ± 0.37
PDRI (5 min)	0.56 ± 0.26	0.60 ± 0.24	1.00 ± 0.34	1.30 ± 0.26	0.88 ± 0.32
Radiographic (x-ray)	0.98 ± 0.28	0.63 ± 0.30	0.87 ± 0.31	0.95 ± 0.20	1.17 ± 0.26
p-value	<0.0001*	0.3545	0.522	0.0003*	0.0044*

*Significant ($p < 0.05$).

registration errors and a relatively smaller registration error for the radiographic registration. However, the difference between the PDRI and radiographic registrations was found to be statistically significant only for 24 mm at $p = 0.0003$. A significant difference between the PDRI and radiographic registration errors was obtained for the 32 mm diameter.

The statistical comparisons of the mean registration error and SD for each source diameter obtained from the PDRI registration at 1, 3, and 5 min and the radiographic registration are shown in figures 8 and 9.

For the diameter of 8 mm, the differences in the registration error for the three acquisition times used in the PDRI registration were found to be statistically significant. However, when compared to the registration error of the radiographic registration, only the 5 min PDRI data yielded a significant difference. The mean registration errors for the image registration

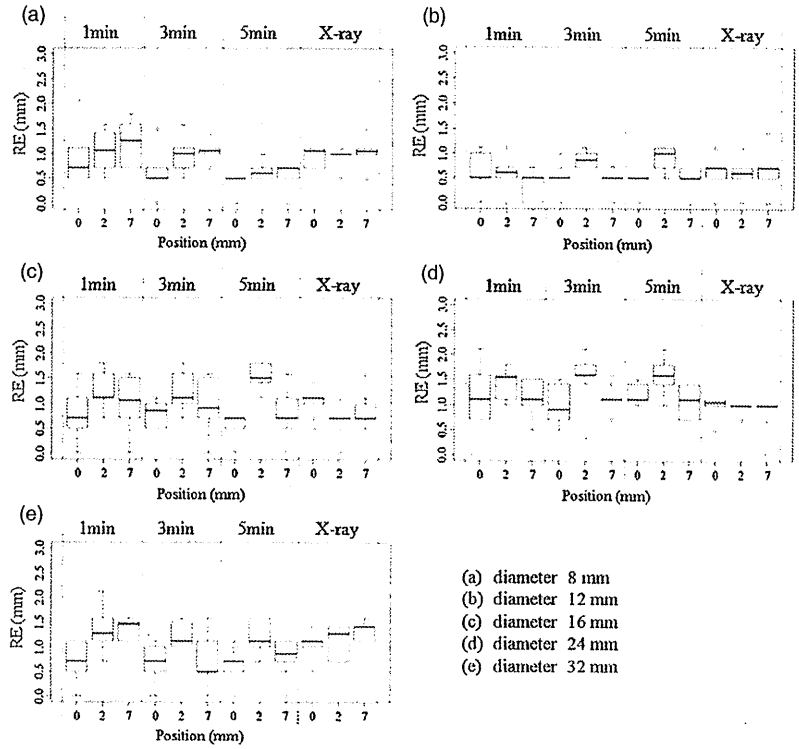

Figure 7. Registration errors for the tumor phantom of figure 3(b). Shown are the results for three phantom positions relative to the isocenter (0), isocenter + 2 mm (2) and isocenter + 7 mm (7) at the acquisition times of 1 , 3 and 5 min, respectively.

conditions shown in figures 8(b) and (c) for diameters of 12 and 16 mm were not statistically different. However, a larger variation in the computed registration error was observed for 16 mm.

For the diameter of 24 mm, the mean registration error obtained for the radiographic registration was found to be significantly smaller compared to those obtained using the PDRI registration method. Furthermore, the acquisition time did not appear to result in significant differences in the mean registration error for the PDRI registration. Like those of the results for the 8 mm diameter, the mean registration error for the 32 mm diameter decreased with the acquisition time in the PDRI registration.

A comparison of the registration error SDs is shown in figure 9 for the various diameters and data acquisition methods. The SDs for most of the results were not statistically different. The image registration SDs of the PDRI at 3 min acquisition time were statistically the same as those of the radiographic registration.

4. Discussion

An overall evaluation of the accuracy of PDRI registration independent of the source size is necessary. We therefore performed a comparative study of the registration error obtained with PDRI and radiographic registrations for a number of hypothetical source sizes. The cumulative

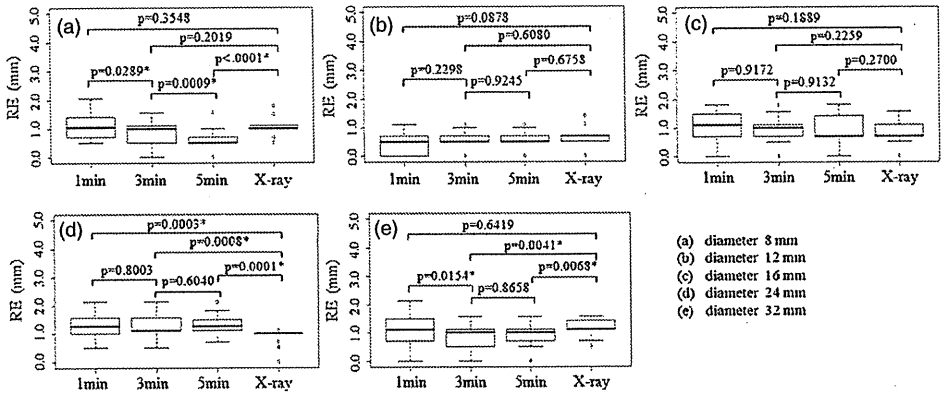

Figure 8. Statistical comparison of the mean registration error for the five cylindrical sources with diameters of 8, 12, 16, 24 and 32 mm using Student's *t*-test at $p < 0.05$ significance level.

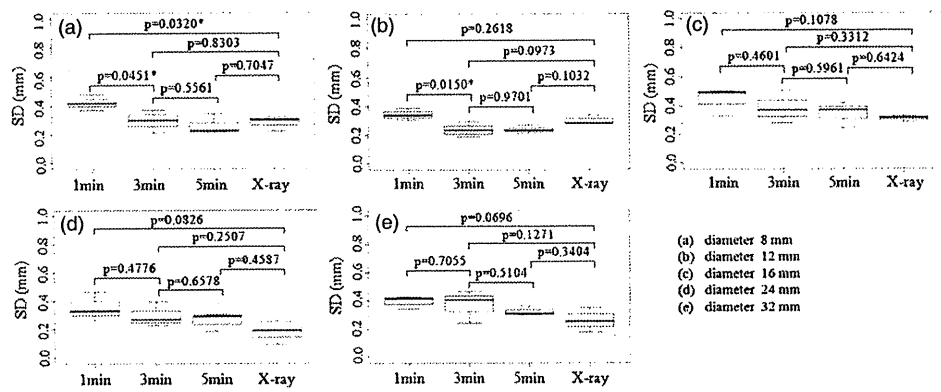

Figure 9. Statistical comparison of the standard deviation of the mean registration error for the five cylindrical sources with diameters of 8, 12, 16, 24 and 32 mm using Student's *t*-test at $p < 0.05$ significance level.

mean registration error and SD for five different source sizes using four registration conditions (i.e. PDRI at 1, 3 and 5 min acquisition times and radiographic registration) are shown in figure 10. A general trend of decreasing mean registration error and SD for longer acquisition time is seen for the PDRI registration. The 3 min data acquisition in the BOLPs yielded comparable results to radiographic registration, while the 5 min acquisition appears to result in lower registration error.

Our tumor phantom experiments show that the mean of the registration errors for the PDRI is approximately 0.93 mm and the SD is approximately 0.33 mm. This is not statistically different from the radiographic registration which had a mean registration error of 0.92 $\pm$ 0.27 mm.

Although there are no reports on the accuracy of image registration using molecular imaging, there have been a number of publications regarding the accuracy of DRR and EPID image registration. Dong and Boyer (1995) showed that in their phantom image registration study, the correlation procedure had a SD of 0.5 mm in aligning translational shifts. Gilhuijs

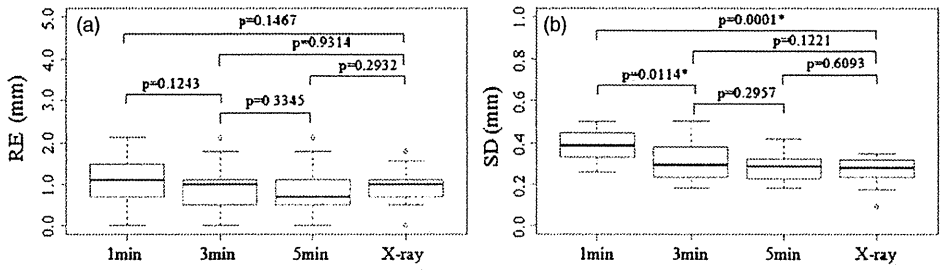

Figure 10. Statistical comparison of (a) the mean registration error and (b) the standard deviation for an overall evaluation using Student's t-test at $p < 0.05$ significance level.

et al (1996) registered 2D portal images with CT data, and their automatic 3D analysis of patient setup accuracy was found to be accurate to within 1 mm in the translational directions. In the clinical evaluation of patient setup errors using portal imaging by Hurkmans *et al* (2001), it was reported that setup errors were less than 2.0 mm (1SD) for head and neck, 2.5 mm (1 SD) for prostate, 3.0 mm (1 SD) for general pelvic and 3.5 mm (1 SD) for lung cancer. The study also noted that the setup verification accuracy varies widely, depending on the treatment site, method of immobilization and institution.

The registration error for the PDRI was lower than that of previously reported radiographic registrations. This could be due to the fact that the image registration was performed with ^{18}F-source itself, not with the skeletal structure, or that there was a phantom dependence. Nevertheless, the registration error for PDRI registration was not significantly different from that of radiographic registration in our experiments. As shown in figure 10(b), the registration error is dependent on the data acquisition time. In order to apply PDRI registration clinically, the acquisition time should be taken into account. A longer acquisition time will result in lower registration error, but it will cause patient discomfort. An optimum acquisition time needs to be considered while maintaining the registration accuracy. However, this is complicated because it depends on the tumor and normal tissue uptake and radiation attenuation in the patient's body. Patient immobilization may also be necessary in order to minimize the effects of inter- and intra-fraction motion caused by patient movement. The effect of respiratory induced motion should be considered in future works.

If FDG is used as the tracer in PDRI registration, it will also be taken up in normal organs such as the brain, liver, kidneys, bladder, etc. This will be a problem in this image registration modality. However, because of the high spatial resolution of our parallel-plane PET system along the in-plane direction, it should be possible to distinguish the tumor FDG uptake from that of the adjacent normal organs which also accumulate FDG. As shown in Figure 4, at the same gantry angle, the corresponding cross-plane image has a much lower resolution and therefore would not be usable for image registration.

Conventional radiographic registration is performed by taking a portal planar image in the LR direction with the gantry at 0° and afterward rotating the gantry to 90° in order to take another portal planar image at the AP direction. These left–right (LR) and anterior–posterior (AP) images are separately registered with corresponding DRR images to complete the radiographic registration process. In our m-IGRT system, the same setup verification procedure using LR and AP images taken separately at different gantry angles will have to be performed. In this case, the PDRI for the LR direction will be the reconstructed in-plane image from the parallel-plane PET data obtained at a gantry angle of 0°. On the other hand, the PDRI for the AP direction will be the reconstructed in-plane image from parallel-plane

PET data obtained at a gantry angle of 90°. The measurement time for each gantry angle is expected to be only a few minutes; therefore, the effects on the acquired parallel-plane PET data of metabolic changes in the body or source activity are negligible.

Additionally, this high spatial resolution will likewise be useful in hypoxic region imaging using FMISO because the hypoxic region distribution in the tumor is complex (Nehmeh *et al* 2008).

5. Conclusion

We performed a basic study to determine the accuracy of image registration using a PET-based molecular image guided method. Planar images were reconstructed from parallel-plane PET data to obtain the PET-based digitally reconstructed planar image (PDRI) used in the registration. In-plane PDRIs had higher resolution and therefore usable for image registration. Phantom experiments using in-plane PDRIs showed that there is no significant difference between radiographic and PDRI registrations. Our results suggest that m-IGRT image registration using PET-based reconstructed planar images along the in-plane direction is feasible for clinical use. Furthermore, the system will provide additional information for image registration when bony structures cannot be recognized with radiographic registration methods.

Acknowledgments

This research was a part of the 'Innovation COE Program for Future Drug Discovery and Medical Care' project and partially supported by the Grant-in-Aid for Special Coordination Funds for Promoting Science and Technology of the Japanese Ministry of Education, Culture, Sports, Science and Technology. The authors are also grateful to the assistance given by the Proton Radiotherapy Department of the National Cancer Center, Kashiwa staff during the experiments with the BOLPs. This research was partially supported by Health and Labour Science Research Grants from the Japanese Government.

References

Dong L and Boyer A L 1995 An image correlation procedure for digitally reconstructed radiographs and electronic portal images *Int. J. Radiat. Oncol. Biol. Phys.* **33** 1053–60

Ford E C, Chang J, Mueller K, Sidhu K, Todor D, Mageras G, Yorke E, Ling C C and Amols H 2002 Cone-beam CT with megavoltage beams and an amorphous silicon electronic portal imaging device: potential for verification of radiotherapy of lung cancer *Med. Phys.* **29** 2913–24

Gilhuijs K G A, van de Ven P J H and van Herk M 1996 Automatic three-dimensional inspection of patient setup in radiation therapy using portal images, simulator images, and computed tomography data *Med. Phys.* **23** 389–99

Groh B A, Siewerdsen J H, Drake D G, Wong J W and Jaffray D A 2002 A performance comparison of flat-panel imager-based MV and kV cone-beam CT *Med. Phys.* **29** 967–75

Hoffman E J *et al* 1989 PET system calibrations and corrections for quantitative and spatially accurate images *IEEE Trans. Nucl. Sci.* **36** 1108–12

Huesman R H *et al* 2000 List-mode maximum-likelihood reconstruction applied to positron emission mammography (PEM) with irregular sampling *IEEE Trans. Med. Imaging* **19** 532–7

Hurkmans C W *et al* 2001 Set-up verification using portal imaging: review of current clinical practice *Radiother. Oncol.* **58** 105–20

Jaffray D A, Siewerdsen J H, Wong J W and Martinez A A 2002 Flat-panel cone-beam computed tomography for image-guided radiation therapy *Int. J. Radiat. Oncol. Biol. Phys.* **53** 1337–49

Lee N Y and Le Q T 2008 New developments in radiation therapy for head and neck cancer: intensity-modulated radiation therapy and hypoxia targeting *Semin. Oncol.* **35** 236–50

Lerche C W *et al* 2005 Depth of γ-ray interaction within continuous crystals from the width of its scintillation light-distribution *IEEE Trans. Nucl. Sci.* **52** 560–72

MacDonald L *et al* 2009 Clinical imaging characteristics of the positron emission mammography camera: PEM Flex Solo II *J. Nucl. Med.* **50** 1666–75

Munbodh R, Jaffray D A, Moseley D J, Chen Z, Knisely J P S, Cathier P and Duncan J S 2006 Automated 2D–3D registration of a radiograph and a cone beam CT using line-segment enhancement *Med. Phys.* **33** 1398–411

Nehmeh S A *et al* 2008 Reproducibility of intratumor distribution of ^{18}F-fluoromisonidazole in head and neck cancer *Int. J. Radiat. Oncol. Biol. Phys.* **70** 235–42

Nishio T *et al* 2005 Distributions of β+ decayed nuclei generated in the CH_2 and H_2O targets by the target nuclear fragment reaction using therapeutic MONO and SOBP proton beam *Med. Phys.* **32** 1070–82

Nishio T *et al* 2006 Dose-volume delivery guided proton therapy using beam online PET system *Med. Phys.* **33** 4190–7

Nishio T *et al* 2010 The development and clinical use of a beam on-line PET system mounted on a rotating gantry port in proton therapy *Int. J. Radiat. Oncol. Biol.Phys.* **76** 277–86

Pouliot J *et al* 2005 Low-dose megavoltage cone-beam CT for radiation therapy *Int. J. Radiat. Oncol. Biol. Phys.* **61** 552–60

Raylman R R *et al* 2008 The positron emission mammography/tomography breast imaging and biopsy system (PEM/PET): design, construction and phantom-based measurements *Phys. Med. Biol.* **53** 637–53

Shepp L A and Vardi Y 1982 Maximum likelihood reconstruction for emission tomography *IEEE Trans. Med. Imaging.* **1** 113–22

Siddon R L 1985 Fast calculation of the exact radiological path for a three dimensional CT array *Med. Phys.* **12** 252–5

Smith M F *et al* 2003 Analysis of factors affecting positron emission mammography (PEM) image formation *IEEE Trans. Nucl. Sci.* **50** 53–9

Smith M F *et al* 2004 Positron emission mammography with tomographic acquisition using dual planar detectors: initial evaluations *Phys. Med. Biol.* **49** 2437–52

Som P *et al* 1980 A fluorinated glucose analog, 2-fluoro-2-deoxy-D-glucose (F-18): nontoxic tracer for rapid tumor detection *J. Nucl. Med.* **21** 670–5

Wienhard K *et al* 2002 The ECAT HRRT: performance and first clinical application of the new high resolution research tomograph *IEEE Trans. Nucl. Sci.* **49** 104–10

Yamaya T, Hagiwara N, Obi T, Yamaguchi M, Kita K, Ohyama N, Kitamura K, Hasegawa T, Haneishi H and Murayama H 2003 DOI-PET image reconstruction with accurate system modeling that reduces redundancy of the imaging system *IEEE Trans. Nucl. Sci.* **50** 1404–9

Zhang J *et al* 2007 Study of the performance of a novel 1 mm resolution dual-panel PET camera design dedicated to breast cancer imaging using Monte Carlo simulation *Med. Phys.* **34** 689–702

JOURNAL OF APPLIED CLINICAL MEDICAL PHYSICS, VOLUME 12, NUMBER 2, SPRING 2011

Proton dose distribution measurements using a MOSFET detector with a simple dose-weighted correction method for LET effects

Ryosuke Kohno,[1,2a] Kenji Hotta,[3,4] Taeko Matsuura,[5] Kana Matsubara,[6] Shie Nishioka,[1,7] Teiji Nishio,[1] Mitsuhiko Kawashima,[1] Takashi Ogino,[1]
National Cancer Center Hospital East,[1] Chiba 277-8577, Japan; National Cancer Center Research Institute,[2] Tokyo 104-0045, Japan; Pure and Applied Sciences,[3] University of Tsukuba, Tsukuba, Ibaraki 305-8577, Japan; Research Fellow of the Japan Society for the Promotion of Science;[4] Department of Medical Physics,[5] Hokkaido University Hospital, Hokkaido 060-8648, Japan; Graduate School of Human Health Sciences,[6] Tokyo Metropolitan University, Tokyo 116-8551, Japan; Foundation for Promotion of Cancer Research,[7] Tokyo, 104-0045, Japan.
rkohno@east.ncc.go.jp

Received 16 August, 2010; accepted 7 January, 2011

We experimentally evaluated the proton beam dose reproducibility, sensitivity, angular dependence and depth-dose relationships for a new Metal Oxide Semiconductor Field Effect Transistor (MOSFET) detector. The detector was fabricated with a thinner oxide layer and was operated at high-bias voltages. In order to accurately measure dose distributions, we developed a practical method for correcting the MOSFET response to proton beams. The detector was tested by examining lateral dose profiles formed by protons passing through an L-shaped bolus. The dose reproducibility, angular dependence and depth-dose response were evaluated using a 190 MeV proton beam. Depth-output curves produced using the MOSFET detectors were compared with results obtained using an ionization chamber (IC). Since accurate measurements of proton dose distribution require correction for LET effects, we developed a simple dose-weighted correction method. The correction factors were determined as a function of proton penetration depth, or residual range. The residual proton range at each measurement point was calculated using the pencil beam algorithm. Lateral measurements in a phantom were obtained for pristine and SOBP beams. The reproducibility of the MOSFET detector was within 2%, and the angular dependence was less than 9%. The detector exhibited a good response at the Bragg peak (0.74 relative to the IC detector). For dose distributions resulting from protons passing through an L-shaped bolus, the corrected MOSFET dose agreed well with the IC results. Absolute proton dosimetry can be performed using MOSFET detectors to a precision of about 3% (1 sigma). A thinner oxide layer thickness improved the LET in proton dosimetry. By employing correction methods for LET dependence, it is possible to measure absolute proton dose using MOSFET detectors.

PACS number: 87.56.-v

Key words: proton, MOSFET detector, LET, simple dose-weighted correction method, *in vivo* dosimetry

I. INTRODUCTION

The Metal Oxide Semiconductor Field Effect Transistor (MOSFET) detector is widely used as a pinpoint dosimeter for photon and electron dose verification.[1-6] The typical design uses

[a] Corresponding author: Ryosuke Kohno, National Cancer Center Hospital East, 6-5-1 Kashiwanoha, Kashiwa-shi, Chiba 277-8577, Japan; phone: +81-4-7133-1111; fax: +81-4-7134-7048; email: rkohno@east.ncc.go.jp

a p-channel enhanced MOSFET constructed on a negatively doped (n-type) silicon substrate. Ionizing radiation generates electron-hole pairs in the insulating layer. The holes drift toward the substrate under an appropriate bias voltage and are semipermanently trapped at the interface, resulting in a shift in the gate voltage required for source-drain conductivity that is proportional to the radiation dose. Following exposure, the gate threshold voltage is measured by applying a constant source-drain current, and the cumulative dose is obtained using suitable calibration factors. The major advantages of this detector include small physical size, the ability to permanently store the accumulated dose, dose-rate and temperature independence, real-time readout, roughly isotropic response for photon beams, and ease of use.

Kohno et al.[7] evaluated the use of the commercially available TN-502RD MOSFET detector with oxide thicknesses of 0.5 μm (Best Medical Canada, Ottawa, Canada) for proton dose measurement. The dose reproducibility, linearity, fading effect and beam intensity dependence were similar to the response obtained from photon beams. On the other hand, Bragg curves measured using the TN-502RD at high bias settings were 20%–40% lower than those measured using an ionization chamber. The MOSFET response is strongly dependent on the degree of linear energy transfer (LET) occurring through columnar recombination. This is due to the significant reduction in charge recombination when the electric field applied to the MOSFET is perpendicular to the plasma track, leading to faster drift of electron-hole pairs. As a result of the LET dependence and the columnar recombination effect, quantitative proton dose measurements are difficult to accurately perform using MOSFET detectors. In order to use a MOSFET detector for proton dosimetry, improved characterization of the response in the Bragg peak region is necessary. Kohno et al.[7] also reported that the response of the TN-502RD was approximately 15% higher than the IC detector at most angles. A lower angular dependence would be desirable when using MOSFET detectors for *in vivo* proton dosimetry.

Cheng et al.[8] investigated another OneDose single use MOSFET detector (Sicel Technologies, Inc., Morrisville, NC) for *in vivo* dosimetry in proton beam therapy. The OneDose detector generally underresponsed compared to the Markus chamber, about 5% at depth of ~ 5 cm, and increase to ≤ 200% at the Bragg peak and beyond. Although it is difficult to measure the Bragg peak with the OneDose, the Cheng study reported that the OneDose provides an opportunity to measure surface dose with proton beam within acceptable clinical criterion of ± 5.0%–6.5%.

In this study, we examined a new MOSFET detector with an oxide thickness of 0.25 μm (TN-252RD) to improve characterization of the MOSFET response for proton beams. The dose sensitivity, angular dependence, and depth-dose response were experimentally evaluated at high bias settings using a 190 MeV proton beam. We also implemented a simple dose-weighted correction method to account for LET dependence suitable for clinical applications. This method was used to perform absolute proton dosimetry using the MOSFET detector.

II. MATERIALS AND METHODS

A. MOSFET dosimetry system

A commercially available MOSFET patient dose verification system (Best Medical Canada, Ottawa, Canada) was used. In order to reduce temperature dependence and nonlinear response at high-dose levels,[9] the dual-MOSFET is composed of two identical MOSFETs, fabricated on the same silicon substrate, with an active area of 0.2×0.2 mm^2. This placement allows for temperature compensation as the two MOSFETs are located on the same substrate. The oxide thickness for the TN-252RD MOSFET is 0.25 μm. The detectors are $2 \times 1.3 \times 8$ mm in size including the encapsulation.[10] All measurements were performed using a high-sensitivity bias voltage setting.

B. Experimental apparatus

B.1 Proton beam setup

Measurements were carried out using the therapeutic proton beam line at the National Cancer Center Hospital East, Japan. The beam line employs the dual-ring double-scattering method for proton therapy.[11] The thickness of the first scatter and the shape of the second scatter are determined by the energy of the proton beams. The maximum size of the irradiation field provided by this system is 200 mm in diameter. The energy of the proton beam was maintained at 190 MeV, and daily testing was used to ensure the proton range was within ± 0.5 mm.[12]

B.2 MOSFET sensitivity and dose calibration

In MOSFET sensitivity (mV/cGy) measurements, the proton energy was 157 MeV at a detector located within a PMMA dose calibration phantom. At this energy the MOSFET detectors displayed no response changes due to LET dependence. A calibrated 0.6 cc Farmer ionization chamber (IC) type 30013 (PTW, Freiburg, Germany) and MOSFET detector were placed along a line perpendicular to the beam axis. The MOSFET and the IC were exposed five times to 200 cGy, and the MOSFET sensitivity was determined from the average output. The sensitivity of the MOSFET detector was also measured using proton beams with energies of 50, 100, 150, 157 and 200 MeV.

For accurate comparisons, the detector outputs were converted to dose values. The dose calibration factor (F_{calib}) in cGy/mV for the MOSFET detector was measured using a 157 MeV proton beam. The raw dose (D_{raw}) for the MOSFET detector was obtained from the product of the MOSFET reading R in mV and the dose calibration factor:

$$D_{raw} = F_{calib} \times R \tag{1}$$

B.3 Angular dependence

The response of MOSFET detectors is dependent on the angle of incidence.[1-5,7] The angular dependence was experimentally evaluated using a cylindrical acrylic phantom with a radius of 8 cm and a length of 15 cm. The angular response with respect to the cable axis was measured at 30°, 45°, 60°, 90°, 120°, 135°, 150°, and 180°.

B.4 Depth-dose curves

Depth-dose curves for mono-energetic proton beams were determined using the IC and MOSFET detectors. Polyethylene (PE) slabs ranging in thickness from 0 to 175 mm were stacked on top of the calibration phantom containing the detectors. The equivalent water thickness was calculated by multiplying the polyethylene thickness by 1.02. The measurements were repeated three times at each thickness, and the results were normalized with respect to the response at a thickness of 0 mm. The ratio of the response of the IC detector to the MOSFET detector was also plotted as a function of thickness. The correction factors (IC/MOSFET) were expressed as a function of the PE thickness (d_{PE}): $cf_{mono}(d_{PE})$.

In actual proton therapy, most patients are treated using a SOBP proton beam created using a ridge-filter. We therefore also measured the depth-dose distribution of an 80 mm SOBP-width proton beam using the MOSFET detector. The ratio of the IC response to the MOSFET response (IC/MOSFET) was obtained and the correction factor cf_{SOBP} was determined as a function of d_{PE} as was done for the mono-energetic proton beam.

C. Dose distribution formed by the protons traversing an L-shaped bolus

C.1 Experimental apparatus

We prepared a polyethylene bolus with an L-shaped horizontal cross section (Fig. 1). The bolus was 50 mm thick at points where $x < 0$ and 10 mm thick when $x \geq 0$. This bolus shape was selected to correspond to the target with large heterogeneity in the lateral direction. Particularly,

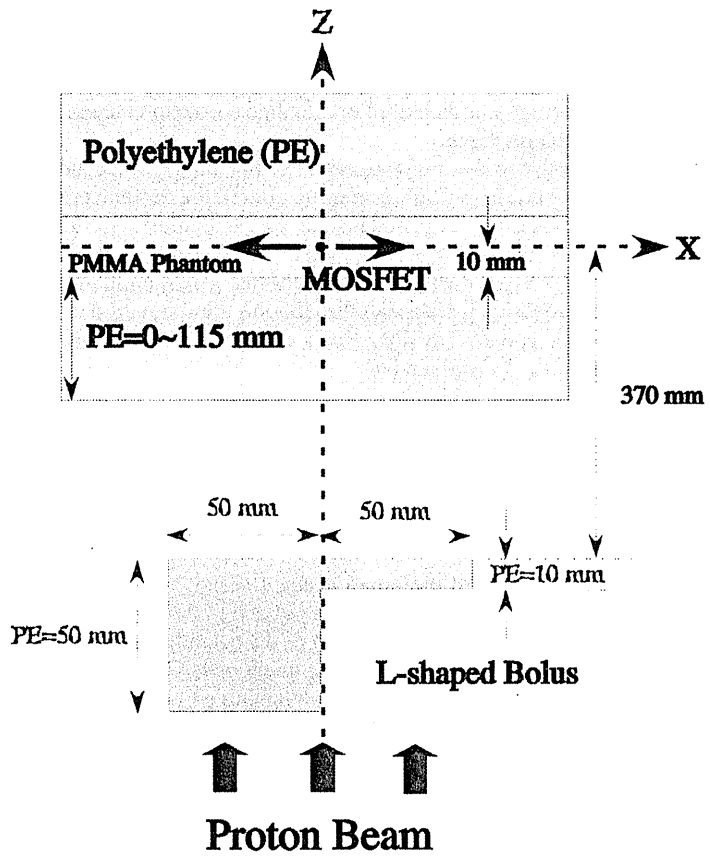

FIG. 1. Experimental arrangement for measurement of dose distribution (top view). The bolus was made of polyethylene.

we expect lateral dose distributions around x = 0 form a complex bump and dip structure due to the bolus edge scattering effect of the bolus region where the thickness changes abruptly. The correction factor of the MOSFET response must take these effects into consideration.

For the 190 MeV mono-energetic proton beam, the Bragg peak positions were 110 mm for protons passing through the thicker section and 150 mm for protons passing through the thinner section. Polyethylene slabs of various thicknesses were stacked on top of the PMMA calibration phantom. The lateral (x-axis) dose distributions were measured using the IC and the TN-252RD MOSFET detector at PE thicknesses of 0, 100, 105, 110 and 115 mm. In addition, we measured the lateral dose distributions at PE thicknesses of 0, 50 and 100 mm for the 80 mm SOBP-width beam.

C.2 A simple dose-weighted correction method

Because of LET dependence, there is a notable disagreement between the IC and the TN-502RD MOSFET detector near the Bragg peak.[7] Knowledge of the LET spectrum is important in cavity theory to account for recombination effects and stopping power ratios.[13] The difference in response cannot be completely explained by differences in stopping power between water and SiO_2. In addition, proton beam therapy uses a spread-out Bragg peak (SOBP) beam containing protons with a range of energies, making it difficult to easily and accurately calculate the LET spectrum at a particular measurement point due to bolus and tissue heterogeneities.

In order to provide a simple correction for the response of the MOSFET detector to various LET effects, we employed a method originally used to correct imaging plate response.[14] A Bragg curve was obtained using the IC detector to establish a standard for the proton beam depth-dose distribution. This curve was then used to calculate correction factors (IC/MOSFET) as a function of proton penetration depth.

The proton penetration depth can be considered as a residual range. Since the protons at any point have a variety of energies due to multiple scattering effects, the residual proton range at an arbitrary point may be calculated using the pencil beam dose calculation algorithm (PBA),[15-17] in which the pencil beam dose distribution is separated into a central-axis term and an off-axis term. The central-axis term represents the measured depth-dose distribution of the broad beam. The off-axis term is a two-dimensional Gaussian distribution the standard deviation of which corresponds to the lateral beam spread. The dose $F(x, y, z, (x_0, y_0))$ delivered by a single pencil beam at an entrance position (x_0, y_0) is given by:

$$F(x,y,z;(x_0,y_0)) = \phi(x_0,y_0)DD(z;(x_0,y_0)) \times \frac{1}{2\pi\sigma(z)^2}\exp\left(-\frac{(x_0-x)^2-(y_0-y)^2}{2\sigma(z)^2}\right), \quad (2)$$

where $\phi(x_0,y_0)$ is the intensity profile of the broad beam, $DD(z;(x_0,y_0))$ is the depth-dose distribution of the broad beam, and $\sigma(z)$ is the proton spread due to multiple scattering effects in the bolus and polyethylene slabs and the configuration of the beam line at z. We can obtain the dose distribution in the region of interest by generating many pencil beams and summing their dose distributions. For dose distributions of protons traversing an L-shaped phantom, Kohno et al.[16] reported the precision of doses calculated using the PBA is approximately 2.5%. The PBA may therefore be considered a precise and practical method for calculating the proton residual range in order to obtain correction factors at arbitrary locations.

The correction factor for the MOSFET response CF(x,y,z) is given by:

$$CF(x,y,z) = \frac{\sum_{i=1}^{n} cf_{dd}(z;(x_i,y_i))F(x,y,z;(x_i,y_i))}{\sum_{i=1}^{n} F(x,y,z;(x_i,y_i))} \quad (3)$$

in which i is the ith pencil beam, n is the total number of pencil beams, (x_i, y_i) is the position of a generated pencil beam, and $cf_{dd}(z;(x_i,y_i))$ is $cf_{mono}(z = d_{PE})$ or $cf_{SOBP}(z = d_{PE})$ (as described in Section B.4 above). The dose measured by the MOSFET detector at (x,y,z), D(x,y,z) may be calculated using:

$$D(x,y,z) = CF(x,y,z) \cdot D_{raw}(x,y,z), \quad (4)$$

where $D_{raw}(x,y,z)$ is the raw dose (as described in Section B.2 above).

Proton dose distributions resulting from an L-shaped bolus (Fig. 1) were measured using the MOSFET and the IC detectors. Protons passing near the abrupt change in thickness at x = 0 displayed a range of energies due to multiple scattering effects, and it was necessary to calculate the proton residual range using the PBA in order to obtain the correction factor.

III. RESULTS & DISCUSSION

A. Dose sensitivity

The sensitivity of the TN-252RD MOSFET detector was 0.72 ± 0.01 (mV/cGy) and the corresponding reproducibility was ± 1.4%. Although the sensitivity of this detector was lower than the TN-502RD MOSFET with a thicker oxide layer, its reproducibility was within 2%. Figure 2 is a graph of the TN-252RD MOSFET sensitivity for each proton energy value. The sensitivities to 150, 157, and 200 MeV proton beams were almost identical, but the sensitivity was reduced at lower proton energies of 100 and 50 MeV.

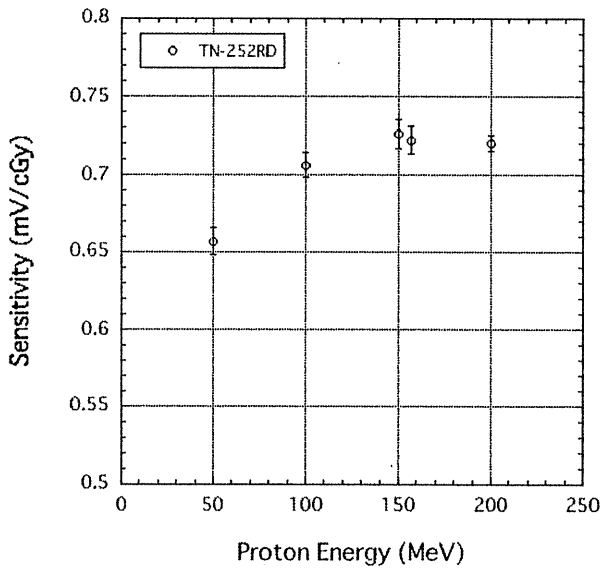

FIG. 2. MOSFET sensitivity for 200, 157, 150, 100 and 50 MeV proton beams.

B. Angular dependence

Figure 3 depicts an angular dependence of the MOSFET detector exposed to a 190 MeV proton beam, and the correction value for the angular response of the MOSFET detector. The electric field is parallel to the incident proton beam when the MOSFET detector is mounted at 0 degrees. The response was normalized to 0°, corresponding to a beam perpendicular to the MOSFET encapsulation epoxy. The angular response at 180° agreed well with the 0° measurements (within ± 2.0%). The TN-252RD detector displayed a maximum overresponse of +9.0%. The overresponse occurs because the fraction of charge pairs escaping recombination increases at larger angles between the electric field and the proton track.[18] Despite the large value, this is a dramatic improvement of almost 10% relative to the TN-502RD device,[7] suggesting that MOSFET detectors constructed using thinner SiO_2 layers exhibit reduced angular dependence. The correction value $CV_{Ang}(\theta)$ may be obtained from the angular response of the TN-252RD detector at a beam angle θ using the relation:

$$CV_{Ang}(\theta) = 1 - 0.00197 \cdot \theta + 0.0000109 \cdot \theta^2. \quad (5)$$

Using this correction value, we can correct the angular response of the TN-252RD MOSFET detector to within 1.5%.

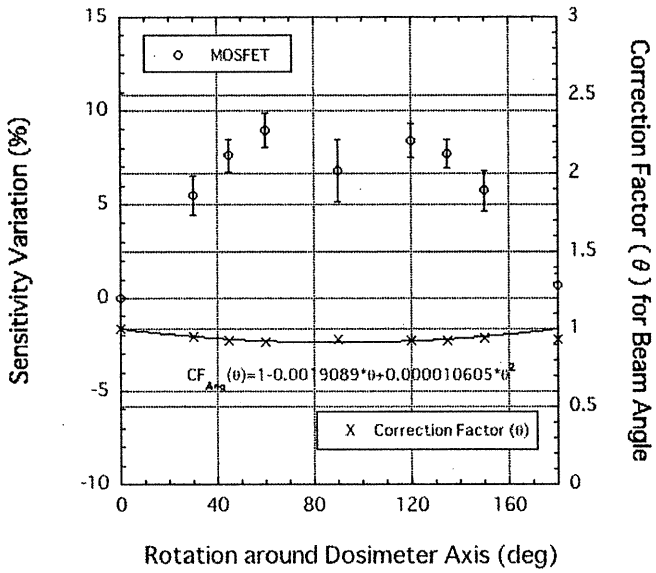

FIG. 3. Angular dependence of MOSFET detectors exposed to a 190 MeV proton beam. The correction value for the angular response of the MOSFET detector is also plotted.

C. Depth-dose curves

Figure 4 shows a comparison of Bragg curves obtained using IC and MOSFET detectors at high-bias setting for a 190 MeV proton beam, and the correction factor for the response of the MOSFET detector was calculated as a function of proton penetration depth. The relative response of the TN-252RD MOSFET detector at the Bragg peak was 0.74. This response relative to the TN-502RD detector[7] also is a larger than a 10% improvement. The correction factor $cf_{mono}(z = d_{PE})$ for the response of the MOSFET detector was determined as a function of proton penetration depth as follows:

$$cf_{mono}(d_{PE}) = \begin{cases} 1 & [d_{PE} < 100.421\,(mm)] \\ 0.781885 + 0.002172 \cdot d_{PE} & [100.421\,(mm) \le d_{PE} < 154.784\,(mm)] \\ -2.94139 + 0.0262266 \cdot d_{PE} & [154.784\,(mm) \le d_{PE}] \end{cases} \quad (6)$$

The MOSFET with the correction agreed well with the IC within 1.5%, as shown in Fig. 4.

A comparison of the SOBP obtained using the IC and MOSFET detectors is shown in Fig. 5. Figure 5 also shows the correction factor for the response of the MOSFET detector was calculated as a function of proton penetration depth. The ratio of the IC and MOSFET (IC/MOSFET) response was also obtained. The correction factor $cf_{SOBP}(d_{PE})$ was expressed as a function of PE thickness using:

$$cf_{SOBP}(d_{PE}) = \begin{cases} 1 & [d_{PE} < 40\,(mm)] \\ 0.94639 + 0.00134025 \cdot d_{PE} & [40\,(mm) \le d_{PE} < 140\,(mm)] \\ 6.59257 - 0.0793194 \cdot d_{PE} + 0.00028807 \cdot d_{PE}^{2} & [140\,(mm) \le d_{PE}] \end{cases} \quad (7)$$

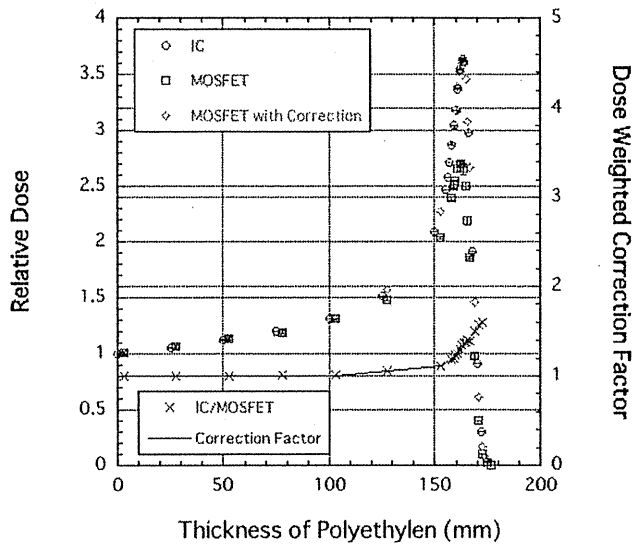

FIG. 4. Comparison of Bragg curves obtained using IC and MOSFET detectors at high-bias setting for a 190 MeV proton beam. The correction factor for the response of the MOSFET detector was calculated as a function of proton penetration depth.

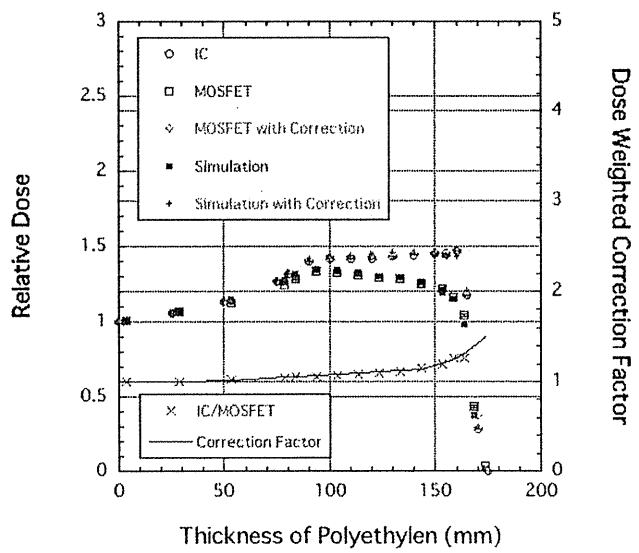

FIG. 5. Comparison of SOBP obtained using IC and MOSFET detectors. The correction factor for the response of the MOSFET detector was calculated as a function of proton penetration depth.

The MOSFET with the correction agreed well with the IC within 1.4%, as shown in Fig. 5.

In this method, $cf_{SOBP}(d_{PE})$ must be measured and calculated for each SOBP width. However, a SOBP distribution may be obtained in a stepwise manner from the dose contributions of mono-energetic proton beams traversing the individual elements of the ridge filter. For example, the "Simulation" curve in Fig. 5 depicts the SOBP distribution obtained using the